https://doi.org/10.5194/egusphere-2026-174
Preprint. Discussion started: 23 February 2026

An Improved Method for Raindrop Size Distribution Retrieval Using Combined Dual-frequency Radar DFR

Liang Feng [1], Jiefan Yang [1] , Zeyong Guo [3,4], Jiming Sun [2], Yue Sun [2], Huiling Yang [2]

[1]State Key Laboratory of Atmospheric Environment and Extreme Meteorology, Institute of Atmospheric Physics, Chinese Academy of Sciences, Beijing 100029, China
[2]Laboratory of Cloud-Precipitation Physics and Severe Storms, Institute of Atmospheric Physics, Chinese Academy of Sciences, Beijing 100029, China
[3]China Meteorological Administration Tornado Key Laboratory, Guangdong, Foshan, 528000, China
[4]Yangjiang Key Laboratory of Meteorological Support for Offshore Economic Industries, Guangdong, Yangjiang, 5295002, China

Correspondence to: Jiefan Yang (yjf@mail.iap.ac.cn)

Abstract. Accurate retrieval of raindrop size distributions (DSDs) is essential for understanding cloud and precipitation microphysics. The dual-frequency ratio (DFR) measured by dual-frequency radars is independent of the normalized intercept parameter (Nw) and depends solely on the mass-weighted mean diameter (Dm). This characteristic makes DFR a powerful parameter for DSD retrieval. However, the DFR-Dm relationship is subject to a dual-solution ambiguity, particularly for smaller particles. In this study, W-band reflectivity is synthetically incorporated through scattering simulations based on measured DSDs, and retrieval relationships are established among X/Ka-band DFR, Ka/W-band DFR, and Dm. The results show that the ambiguity in the DFR-Dm relationship is substantially reduced, and the proposed method demonstrates clear advantages over conventional approaches, especially when retrieving DSDs of weak echoes. This advancement effectively addresses a key gap in the measurement and analysis of light precipitation processes.

1 Introduction

As a fundamental parameter in cloud and precipitation microphysics, the raindrop size distribution (DSD) characterizes the size distribution of precipitation particles (Marshall and Palmer, 1948; Ulbrich, 1983; Testud et al., 2001). Accurate retrieval of DSD is crucial for advancing research in cloud and precipitation microphysics, developing and evaluating cloud microphysics schemes in numerical models, supporting weather modification activities, and understanding cloud–climate interactions (Liu et al., 2021). Consequently, how to accurately retrieve DSD has always been an important research topic in radar meteorology. However, due to the variability in precipitation particle shape, density, size, orientation, and spectral characteristics, accurately quantifying the microphysical properties of cloud and precipitation systems using single-frequency radar remains a significant challenge (Li et al., 2023).

https://doi.org/10.5194/egusphere-2026-174
Preprint. Discussion started: 23 February 2026

Numerous studies have demonstrated that the dual-frequency radar could retrieve DSD more accurately with the Dual-Frequency Ratio (DFR) (Seto et al., 2013; Liao and Meneghini, 2019a; Kubota et al., 2020). This technique employs two distinct wavelengths: one is chosen such that Rayleigh scattering dominates for most precipitation-sized particles, while the other is sufficiently short to trigger Mie scattering in the presence of large hydrometeors (Liao and Meneghini, 2019b). Since Mie scattering is more sensitive to particle size, an increase in particle diameter amplifies the difference in scattering characteristics between the two frequencies, resulting in a noticeable increase in DFR. This makes DFR a key diagnostic parameter for characterizing the DSD.

Another important advantage of the DFR is its independence on the normalized intercept parameter (Nw) when retrieving the DSD. Under the normalized gamma size distribution assumption with a fixed shape factor (μ), DFR depends only on the mass-weighted mean diameter (Dm). Meneghini et al. (2022) demonstrated that the retrieved DSD closely matches in situ observations when μ is set to 3. Most studies on DFR-based DSD retrieval have focused on the dual-frequency Ku/Ka-band radar aboard the Global Precipitation Measurement (GPM) satellite (Hou et al., 2014; Liao et al., 2014; Skofronick-Jackson et al., 2017, 2018; Iguchi et al., 2021; Seto et al., 2021; Iguchi and Meneghini, 2022; Ladino-Rincon et al., 2025).

A great challenge in DFR-based DSD retrieval is the DFR–Dm dual-solution. For example, when DFR ≤ 0, a single DFR value corresponds to two Dm values (Meneghini et al., 1992, 1997; Mardiana et al., 2004; Liao and Meneghini, 2005; Rose and Chandrasekar, 2005). A commonly used approach is to select the large Dm value as the solution, which often introduces retrieval errors, particularly in light precipitation (Mardiana et al., 2004; Meneghini et al., 2022). Another method is to discard data with DFR ≤ 0 and only use data with DFR > 0 to retrieve Dm, which results in considerable data loss (Wang et al., 2020; Liu et al., 2020).

To address the DFR–Dm dual-solution, Liao and Meneghini (2019) proposed a generalized dual-frequency ratio, denoted as DFR* (DFR* = $dBZ(f_1) - \gamma \cdot dBZ(f_2)$, where $\gamma \in [0, 1]$). Although DFR* successfully avoids the ambiguity inherent in the original DFR formulation, it is no longer a function solely of Dm and introduces a dependence on Nw. Iguchi and Meneghini (2022) further introduced a retrieval approach based on the differential form of the dual-frequency radar equation, investigating the stability of Dm retrievals with respect to variations in initial conditions. However, this method primarily mitigates the dual-solution under conditions of strong attenuation (i.e., intense precipitation). Meneghini et al. (2022) also noted that it is not always possible to identify the correct solution among multiple candidates although the DFR–Dm dual-solution can be addressed analytically. Given that the dual-solution in the DFR-Dm relationship has not been adequately resolved, the GPM currently employs the R-Dm relationship to retrieve Dm (Seto et al., 2021).

This paper is structured as follows: Section 2 introduces the theoretical background of the DFR-Dm relationship, and the overall DSD retrieval strategy. Section 3 presents the preprocessing steps, including attenuation correction and the construction of the retrieval algorithm based on scattering simulation. Section 4 provides a comprehensive evaluation of the proposed method using both case studies and ground-based disdrometer validation. Finally, Section 5 summarizes the key findings discusses limitations, and outlines directions for future research.

https://doi.org/10.5194/egusphere-2026-174
Preprint. Discussion started: 23 February 2026

2 Overall retrieval strategy

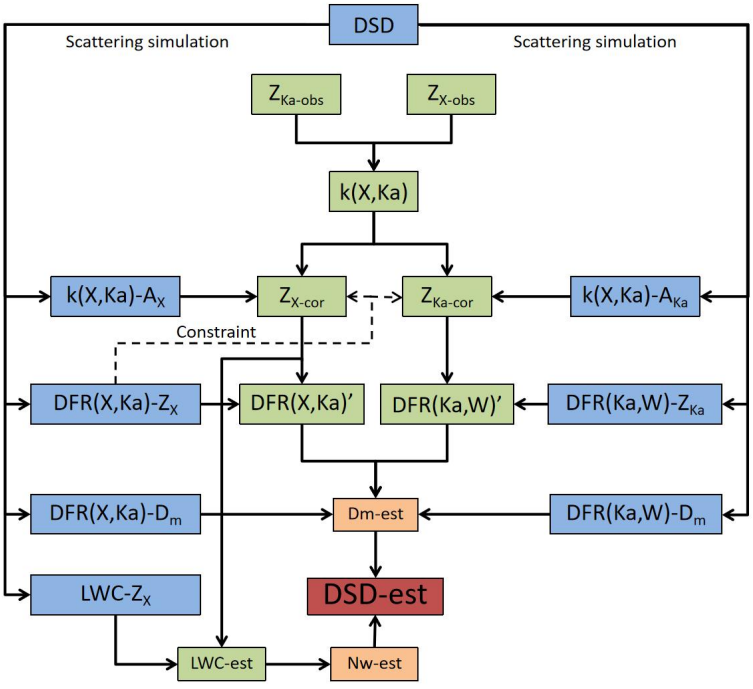

Figure 1. X/Ka dual-frequency radar raindrop size distribution retrieval schematic.

This study proposes a solution to the ambiguity of DFR-Dm by T-matrix scattering simulation. The overall retrieval frame work is shown in Fig. 1. The core concept of this method is rooted in the physical principle that the DFR at distinct frequency pairs, specifically X/Ka and Ka/W bands, exhibits distinct responses to variations in Dm. This disparity arises from differences in their sensitivity to particle size and scattering regime.

In the DFR(X, Ka)-Dm relationship, the dual-solution means a single DFR corresponds to two Dm values when DFR(X, Ka)≤0. This ambiguity severely limits the applicability of DSD retrieval method based on DFR. To resolve the ambiguity, the DFR(Ka, W) is employed, which operates at higher frequencies. Our analysis shows that the ambiguity of DFR(Ka, W)-Dm is significantly narrower than that of DFR(X, Ka)-Dm. This allows DFR(Ka, W) to resolve the ambiguity of DFR(X, Ka)-Dm.

The analysis reveals that DFR(Ka, W)-Dm effectively resolves the large Dm (>0.5 mm) when DFR(X, Ka) is less than 0, while the residual errors associated with small Dm (≤0.5 mm) are almost negligible. Additionally, due to the divergence of corrected reflectivity when applying differential specific attenuation (k(X,Ka)) to correct reflectivity at X/Ka-bands, this study constrains the corrected reflectivity using the DFR(X, Ka)-Z_X relationship derived from scattering simulation.

https://doi.org/10.5194/egusphere-2026-174
Preprint. Discussion started: 23 February 2026

3 Instrument and Data Processing

3.1 Instruments

The dataset utilized in this study comprises radar observations from an X/Ka dual-frequency vertically pointing radar and drop size distribution measurements from a 2-dimensional video disdrometer (2DVD). Both datasets were collected at the meteorological observation site in Yangjiang, Guangdong Province, on May 1, May 11, June 11, 2022 and June 14, 2025. The X/Ka dual-frequency radar, developed by the 38th Research Institute of China Electronics Technology Group Corporation (CETC-38), employs a fully solid-state frequency-modulated continuous wave (FMCW) system. Its high temporal and spatial resolution enables the real-time tracking of precipitation system structural evolution. The 2DVD, developed by Austria's Joanneum Research, is designed to capture the two-dimensional size distribution and phase characteristics of precipitation particles. It provides essential ground-truth data for DSD research and phase identification algorithm validation. The main technical specifications of the X/Ka-band radar are presented in Table 1.

Table 1. Key specifications of X/Ka dual-frequency radar system

Paremeters	Specification
Operating Frequency	35.02 GHz(Ka-band) ; 9.37 GHz (X-band)
Antenna Diameter	1864 mm
Antenna Gain	54.6 dB (Ka-band); 44.6 dB (X-band)
Beamwidth	0.4° (Ka-band); 1° (X-band)
Range Resolution	≤ 30 m
Detection Capability	≤-38dBZ@10km(Ka-band); ≤-25dBZ@10km(X-band)
Measured Variables	Z, V, W, Z_{DR}, Φ_{DP}, K_{DP}, ρ_{HV}
Accuracy	Z ≤1.0 dBZ; V ≤ 1.0 m s^{-1}; W ≤ 1.0 m s^{-1}; Z_{DR} ≤ 0.2 dB; Φ_{DP} ≤ 1°; K_{DP} ≤ 0.2° km^{-1}; ρ_{HV} ≤ 0.01

As shown in Table 1, the mismatch in beamwidth between the X- and Ka-band leads to scale errors. The scale errors can be reduced by time averaging and spatial smoothing (Ellis and Vivekanandan, 2011). In this study, Ka-band reflectivities were smoothed along the time dimension using a moving average with a 3-point window. Through data processing, the beam width of the Ka-band was adjusted to 1.2°, closely matching that of the X-band.

3.2 DSD Parameters

The DSD is assumed to follow the normalized gamma size distribution (Testud et al. 2001):

$$N(D) = N_W f(\mu)\left(\frac{D}{D_m}\right)^{\mu} exp\left[\frac{-(4+\mu)D}{D_m}\right] \quad (1)$$

$$f(\mu) = \frac{6(4+\mu)^{\mu+4}}{4^4\Gamma(\mu+4)} \quad (2)$$

https://doi.org/10.5194/egusphere-2026-174
Preprint. Discussion started: 23 February 2026

where Nw is the normalized intercept parameter, μ is the shape factor, Γ denotes the gamma function, and D is the raindrop diameter. The n-th moment of the DSD can be obtained by integrating the spectrum, as defined by Tokay and Beard (1996):

$$M_n = \int_{D_{min}}^{D_{max}} D^n N(D) dD \tag{3}$$

The subscripts min and max represent the minimum and maximum diameters of raindrops, respectively. Parameters such as Dm, liquid water content (LWC), and Nw can be derived from the moments of the DSD:

$$D_m = \frac{M_4}{M_3} = \frac{\int_{D_{min}}^{D_{max}} D^4 N(D) dD}{\int_{D_{min}}^{D_{max}} D^3 N(D) dD} \tag{4}$$

$$LWC = \frac{\pi}{6} M_3 = \frac{\pi}{6} \times 10^{-3} \int_0^{\infty} D^3 N(D) dD \tag{5}$$

$$Nw = \frac{4^4}{\pi \rho_w} \left(\frac{LWC}{D_m^4} \right) \tag{6}$$

where ρ_w is water density.

3.3 Scattering Simulation

The T-matrix method provides an efficient and rigorous approach for computing electromagnetic scattering by nonspherical particles, which was developed by Waterman (1965, 1971). By directly solving Maxwell equations with appropriate boundary conditions, the method is particularly suitable for modeling the scattering properties of axisymmetric hydrometeors, such as raindrops, snowflakes, and graupel. In this study, the T-matrix method is employed to simulate the scattering characteristics of measured raindrop size distributions at X-, Ka-, and W-band frequencies. The simulations serve as the theoretical foundation for developing a new DSD retrieval algorithm based on dual-frequency radar observations.

In the context of radar meteorology, the radar reflectivity is defined as follows (in units of $mm^6 \cdot m^{-3}$):

$$Z_{h,v} = \frac{\lambda^4}{\pi^5} \left| \frac{m^2+2}{m^2-1} \right| \int_{D_{min}}^{D_{max}} \sigma_{H,V}(D) N(D) dD \tag{7}$$

where λ is the wavelength of the electromagnetic wave, m is the complex refractive index of the precipitation particle, and $\sigma_{H,V}$ denotes the horizontal or vertical backscattering cross section. $Z_{h,v}$ represents the horizontal or vertical radar reflectivity. When expressed in terms of T-matrix elements, the Eq. (7) becomes:

$$Z_h = Cn_0 \langle \sigma_H \rangle = 2\pi Cn_0 \langle \overline{M}_{11} - \overline{M}_{12} - \overline{M}_{21} + \overline{M}_{22} \rangle \tag{8}$$

$$Z_v = Cn_0 \langle \sigma_V \rangle = 2\pi Cn_0 \langle \overline{M}_{11} + \overline{M}_{12} + \overline{M}_{21} + \overline{M}_{22} \rangle \tag{9}$$

where $\langle \dots \rangle$ denotes the volumetric ensemble average of the phase matrix elements for precipitation particles, and no represents the total number of particles per cubic meter. The constant C is defined as $C = 10^{18} \lambda^4 / (\pi^5 |K|^2)$, where $K = (\varepsilon - 1)/(\varepsilon + 2)$, and ε is the dielectric constant of the hydrometeor, given by $\varepsilon = m^2$. These parameters are derived from the phase matrix outputs of T-matrix scattering simulations (Feng et al., 2019).

https://doi.org/10.5194/egusphere-2026-174
Preprint. Discussion started: 23 February 2026

Due to the influence of aerodynamic drag, raindrops typically deform into an oblate shape, where the horizontal axis is longer than the vertical axis. This anisotropic geometry leads to polarization-dependent variations in radar backscatter characteristics that are sensitive to the radar observation angle. Specifically, when the radar scans at low elevation, the horizontally polarized reflectivity generally exceeds the vertically polarized reflectivity, producing a positive differential reflectivity (Z_{DR}) that serves as an important microphysical indicator of drop shape and size distribution. Conversely, for vertically pointing radars, the symmetry of the observation geometry with respect to the oblate drops effectively eliminates polarization-dependent differences, resulting in nearly equal reflectivities for both horizontal and vertical polarizations ($Z_H \approx Z_V$). This characteristic underpins the interpretation of radar measurements and dictates the choice of retrieval algorithms depending on the scanning strategy and precipitation microphysics.

In this study, the raindrop axis ratio is determined using the following relationship (Tang et al., 2014):

$$r = 0.9971 + 0.2193D - 3.5105D^2 + 5.0746D^3 - 2.3559D^4 \quad (10)$$

Table 2. Complex refraction index of raindrops at X-, Ka-, and W-band at different temperatures.

Frequency/GHz	Temperature	Complex refraction index
X（9.37）	0℃	7.1421 - 2.8658*i
	10℃	7.6978 - 2.4756*i
	20℃	8.0227 - 2.0341*i
	30℃	8.1539 - 1.6212*i
Ka（33.44）	0℃	4.0271 - 2.4779*i
	10℃	4.5744 - 2.6973*i
	20℃	5.1486 - 2.8070*i
	30℃	5.7062 - 2.7885*i
W（93.75）	0℃	2.7370 - 1.3762*i
	10℃	2.9711 - 1.6413*i
	20℃	3.2455 - 1.8876*i
	30℃	3.5639 - 2.1095*i

The vertically pointing radar is configured with a zenith angle of 0°, ensuring a perfectly nadir (vertical) observation geometry. The complex refractive indices of raindrops at the X-, Ka-, and W-band frequencies at 0-30℃ used in the scattering simulations are summarized in Table 2 (Chang and Wilheit, 1979; Liebe, 1985).

To evaluate the impact of temperature on raindrop size distribution retrieval, we take DFR(Ka,W) as an example to simulate the retrieved relationship between DFR(Ka,W) and Dm for raindrops at different temperatures (Fig. 2). As can be seen from the figure, the retrieved Dm decreases with increasing temperature, but the retrieval error is relatively small. In this study, we established the DFR-Dm retrieval model with 20°C as the reference temperature.

https://doi.org/10.5194/egusphere-2026-174
Preprint. Discussion started: 23 February 2026

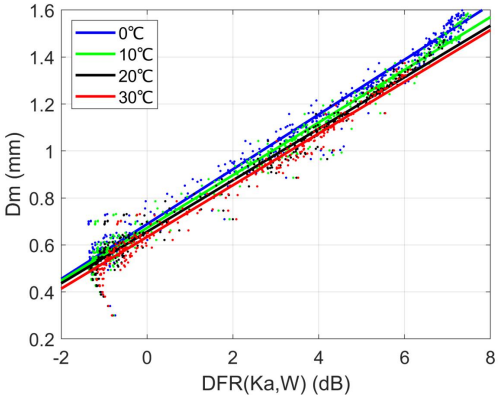

155 Figure 2. Retrieved fitting curves of DFR(Ka,W)-Dm at different temperatures (blue: 0°C; green: 10°C; black: 20°C; red: 30°C).

3.4 Attenuation correction

The profiles of reflectivity measured by the X/Ka dual-frequency vertically pointing radar are shown in Fig. 3. Since both X- and Ka-band signals are subject to rain-induced attenuation, attenuation correction must be applied to the observed
160 reflectivity prior to DSD retrieval.

https://doi.org/10.5194/egusphere-2026-174
Preprint. Discussion started: 23 February 2026

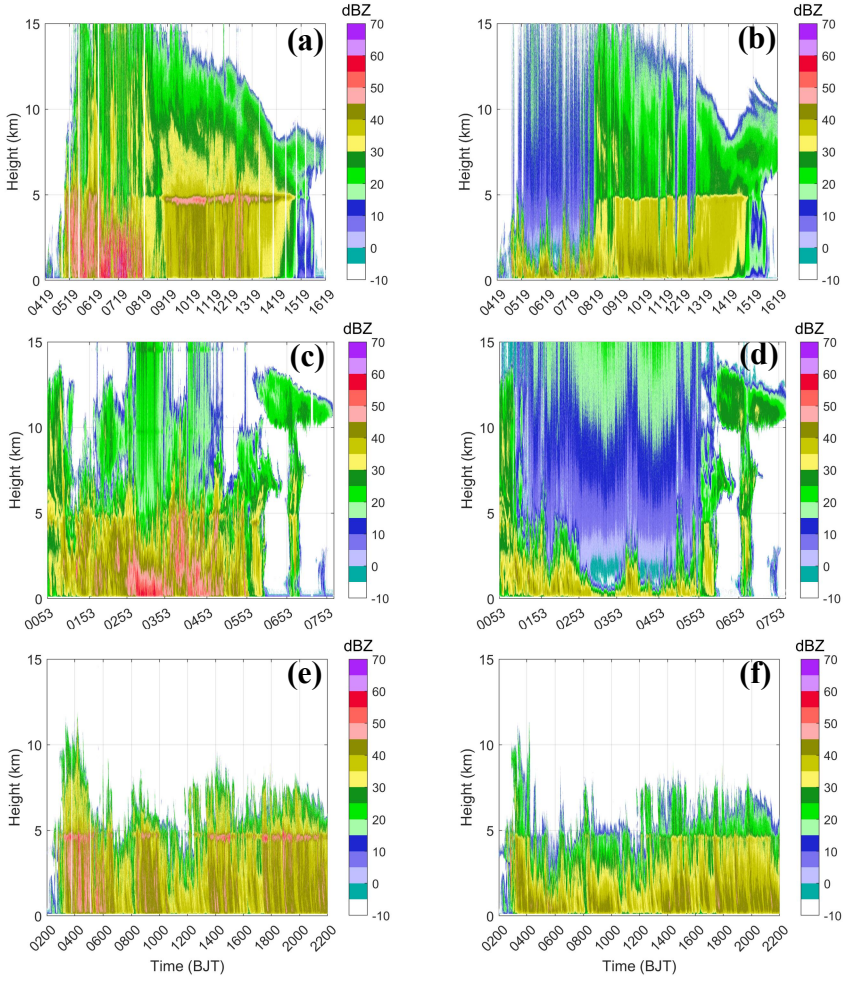

Figure 3. Time-height indicator of the dual-frequency radar reflectivity (X-band: a, c, e; Ka-band: b, d, f; top row: June 11, 2022; middle row: May 11, 2022; bottom row: May 1, 2022).

In order to ensure comprehensive coverage of various precipitation types, we utilizes observation data from May 1 and 11, 2022, June 11, 2022, and June 14, 2025. The 2022 datasets are employed to construct the raindrop size distribution retrieval model, while the observation data from June 14, 2025, serve for model validation. The case on May 1, 2022 was dominated by stratiform precipitation, while the case on May 11, 2022 was dominated by convective precipitation. The June 11, 2022 case evolved from convective to stratiform precipitation as the convective activity gradually weakened.

Taking the case on June 11, 2022 as an example, the X-band exhibits less attenuation than the Ka-band. As a result, a pronounced bright band near the melting layer is evident at X-band in the stratiform precipitation (Fig. 3a), whereas the corresponding feature is barely discernible at Ka-band (Fig. 3b). Junyent et al. (2019) found that Mie scattering at X-band becomes significant only when raindrop diameters exceed approximately 6 mm. Chudler et al. (2022) found that raindrops exceeding 4.5 mm in diameter primarily form through the melting of hail and graupel, not the warm-rain process. As no hail

https://doi.org/10.5194/egusphere-2026-174
Preprint. Discussion started: 23 February 2026

or graupel was observed during either event, Mie scattering at X-band is expected to be negligible. Therefore, the X-band reflectivity is primarily influenced by rain attenuation, while Ka-band reflectivity is affected by both attenuation and Mie scattering.

Figure 4 shows the ground-measured rain rate, Dm and Nw for the three precipitation events, including both extreme precipitation with hourly rain rate exceeding 100 mm h^{-1} (Fig. 4a: 0519-0719 BJT; Fig. 4b: 0253-0453 BJT) and stable stratiform precipitation (Fig. 4a: 0819-1019 BJT; Fig. 4c: 0800-2200 BJT).

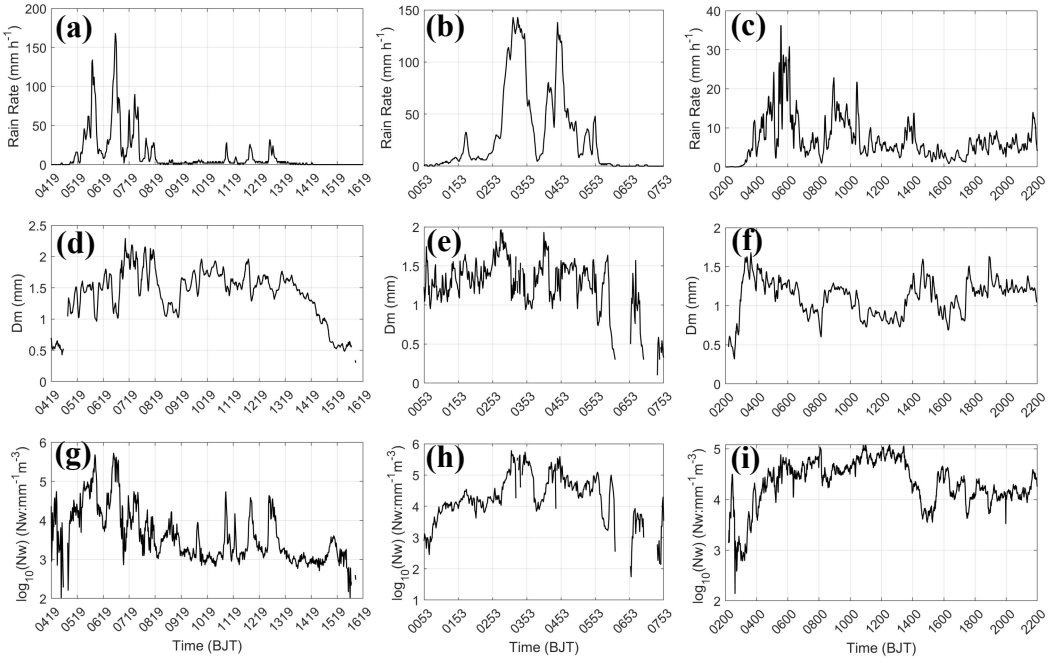

Figure 4. Time series plots of ground-observed rain rate (a-c), mass-weighted mean diameter (Dm, d-f), and normalized intercept parameter (Nw, g-i). (left: June 11, 2022; middle: May 11, 2022; right: May 1, 2022).

The X/Ka reflectivity is corrected for attenuation by applying the differential specific attenuation (Meneghini et al., 1992). The differential specific attenuation of the X/Ka-band is defined as:

$$k(X,Ka) = \frac{[Z_X(r_2) - Z_{Ka}(r_2)] - [Z_X(r_1) - Z_{Ka}(r_1)]}{2(r_2 - r_1)} \quad (11)$$

where r_1, r_2 represent the near and far ends of the radar beam path, respectively. $Z_{Ka}(r_1)$ and $Z_{Ka}(r_2)$ denote the Ka-band reflectivity at the near and far ranges, while $Z_X(r_1)$ and $Z_X(r_2)$ denote the corresponding X-band reflectivity. The relationships between the specific attenuation at X-band (A_X), Ka-band (A_{Ka}), and k(X, Ka) are estimated by scattering simulation based on measured DSDs (Fig. 5).

https://doi.org/10.5194/egusphere-2026-174
Preprint. Discussion started: 23 February 2026

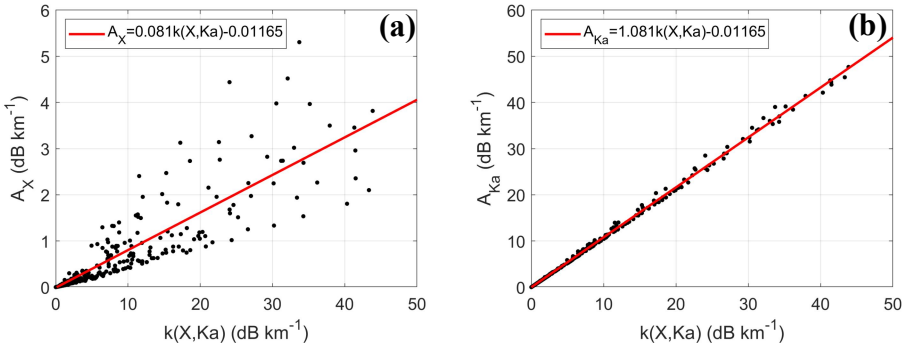

Figure 5. Scatterplots of the differential specific attenuation [k(X,Ka)] and specific attenuation (a: A_X, b: A_{Ka}).

The differential specific attenuation formula provides accurate results when hydrometeors are relatively small and Mie scattering is negligible at both X- and Ka-band. However, in the presence of larger particles where Mie scattering becomes significant at Ka-band, the differential specific attenuation tends to be overestimated, leading to inflated values of A_X and A_{Ka}. To address this, the attenuation correction procedure for X/Ka dual-frequency radar should be constrained by theoretical DFR(X, Ka) values obtained from fitted scattering simulation results.

Furthermore, to reduce the ambiguity of DFR(X, Ka)-Dm, theoretical DFR(Ka, W) are similarly obtained and used to retrieve Dm when DFR(X, Ka) is less than 0 (Section 3.6). The scattering simulation results and fitted curves are illustrated in Fig. 6, and the corresponding polynomial coefficients are listed in Table 3.

$$y = p_1x^6 + p_2x^5 + p_3x^4 + p_4x^3 + p_5x^2 + p_6x + p_7 \quad (12)$$

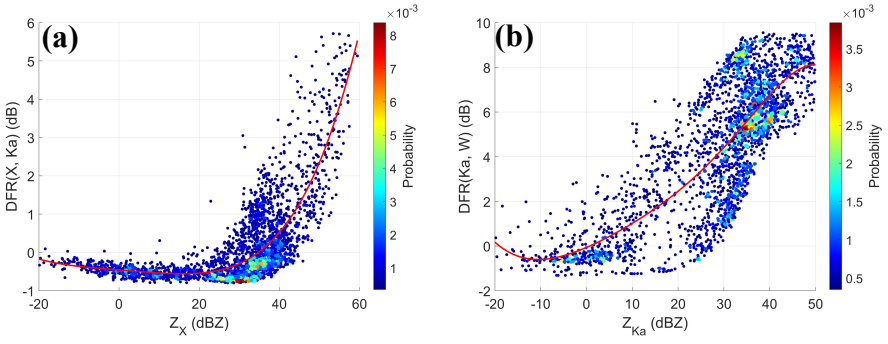

Figure 6. Scatterplots of the X-band reflectivity (Z_X) and X/Ka dual-frequency ratio [DFR(X, Ka)]; the Ka-band reflectivity (Z_{Ka}), and Ka/W dual-frequency ratio [DFR(Ka, W)].

Table 3. Coefficients of the fitted polynomial

coefficients	Z_{Ka}-DFR(Ka, W)	Z_X-DFR(X, Ka)
p1	-4.823×10-10	0
p2	-8.014×10-9	0
p3	2.746×10-6	5.456×10-7

https://doi.org/10.5194/egusphere-2026-174
Preprint. Discussion started: 23 February 2026

p4	-7.539×10-5	-2.216×10-6
p5	2.419×10-3	3.618×10-5
p6	8.842×10-2	-8.324×10-3
p7	-6.192×10-2	-4.585×10-1

Since this study focuses on retrieving raindrop size distributions, all figures presented herein display physical parameters exclusively below the melting layer. As shown in Figure 7, the corrected reflectivities at X- and Ka-band exhibit improved consistency within weak echo regions. In contrast, within strong echo zones, the corrected X-band reflectivity exceeds that at Ka-band, which aligns with theoretical expectations that the dual-frequency ratio increases with reflectivity. Additionally, a bright band feature is evident near the melting layer in the corrected Ka-band reflectivity (Fig. 7b). A similar effect was observed on 1 May 2022 (Fig. 7f), further supporting the physical consistency and accuracy of the attenuation correction.

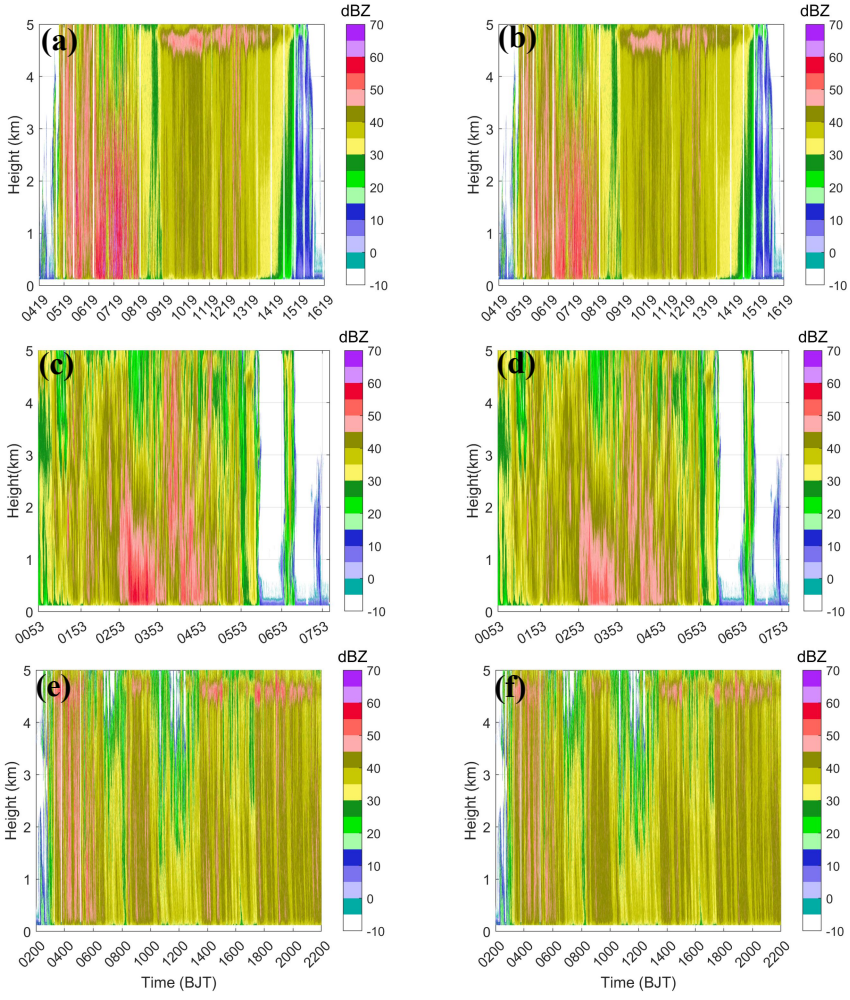

https://doi.org/10.5194/egusphere-2026-174
Preprint. Discussion started: 23 February 2026

Figure 7. Corrected reflectivity of the dual-frequency radar (X-band: a, c, e; Ka-band: b, d, f; top: June 11, 2022; middle: May 11, 2022; bottom: May 1, 2022).

The corrected reflectivities were validated against those derived from ground-based raindrop size distributions measurements. The X/Ka dual-frequency radar begins recording at the fourth gate (gate length: 30 m) and the reflectivity at 120 m is taken as an approximation of the ground-level value. As shown in Figure 8a, the X-band reflectivity exhibits negligible attenuation and closely agrees with the values calculated from raindrop size distributions. While the Ka-band reflectivity suffers marked attenuation (especially above 30 dBZ, Fig. 8b), the corrected results demonstrate close agreement with theoretical values.

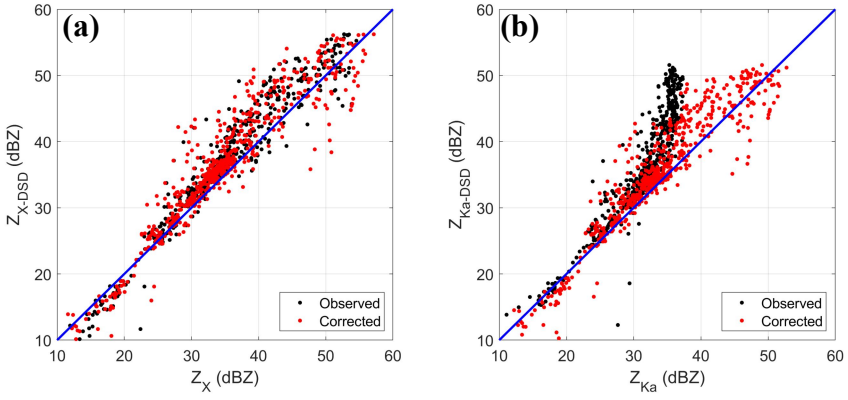

Figure 8. The comparison between the observed and corrected reflectivity values for X-band (Z_X) and Ka-band (Z_{Ka}) at 120m height and the corresponding reflectivity derived from measured raindrop size distributions ($Z_{X\text{-}DSD}$, $Z_{Ka\text{-}DSD}$).

The performance of the attenuation correction was quantitatively evaluated using the mean bias (MB), mean absolute error (MAE), root mean square error (RMSE) and correlation coefficient (CC), defined as follows:

$$MB = \frac{1}{n}\sum_{i=1}^{n}(E_i - T_i) \tag{13}$$

$$MAE = \frac{1}{n}\sum_{i=1}^{n}|E_i - T_i| \tag{14}$$

$$RMSE = \sqrt{\frac{1}{n}\sum_{i=1}^{n}(E_i - T_i)^2} \tag{15}$$

$$CC = \frac{\sum_{i=1}^{n}(E_i-\overline{E})(T_i-\overline{T})}{\sqrt{\sum_{i=1}^{n}(E_i-\overline{E})^2}\sqrt{\sum_{i=1}^{n}(T_i-\overline{T})^2}} \tag{16}$$

where E_i is the observed or corrected value, T_i is the true value, $\overline{E}$ and $\overline{T}$ is the mean value, and n is the total sample size.

As presented in Table 4, the corrected Ka-band reflectivity ($Z_{Ka\text{-}cor}$) aligns much more closely with theoretical values than the observed reflectivity ($Z_{Ka\text{-}obs}$). This improvement is evidenced by a significant reduction in MB, along with decreased MAE and RMSE, and an increased CC.

https://doi.org/10.5194/egusphere-2026-174
Preprint. Discussion started: 23 February 2026

Table 4. Error statistics of Ka-band reflectivity before and after correction

Parameter	MB (dB)	MAE (dB)	RMSE (dB)	CC
$Z_{Ka\text{-}obs}$	-5.2206	5.4504	7.5531	0.9017
$Z_{Ka\text{-}cor}$	0.1720	3.0525	4.9096	0.9413

Using the accurately corrected X- and Ka-band reflectivity, the DFR(X, Ka) and DFR(Ka, W) are obtained (Fig. 9). The results show that DFR(Ka, W) has a broader dynamic range than DFR(X, Ka), and regions of high values coincide for both ratios.

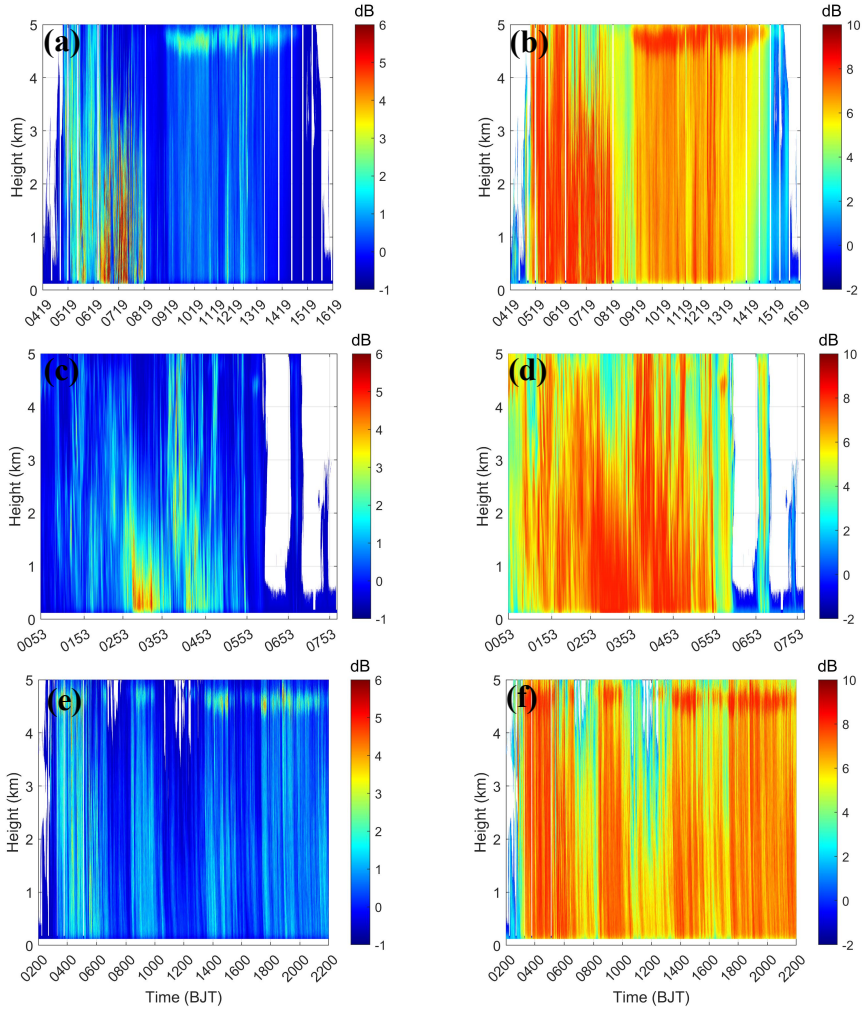

Figure 9. Time-height indicator of the dual-frequency ratio [DFR(X,Ka): a, c, e; DFR(Ka,W): b, d, f; top row: June 11, 2022; middle row: May 11, 2022; bottom row: May 1, 2022].

https://doi.org/10.5194/egusphere-2026-174
Preprint. Discussion started: 23 February 2026

3.5 Sensitivity analysis of μ

The setting of the shape parameter (μ) can influence the retrieval results. To minimize retrieval errors, the optimal value of μ was determined through sensitivity tests. As shown in Figure 10a, the retrieval error for Dm is largest when μ = -3. The error gradually increases as μ takes values of 0, 3, and 6, though the differences among these cases are not significant. Figure 10b shows that the retrieval error for Nw decreases progressively as μ increases. The corresponding statistical results are summarized in Table 5. Based on a comprehensive evaluation of these findings, μ was set to 3 in this study, consistent with the value adopted by Meneghini et al. (2022).

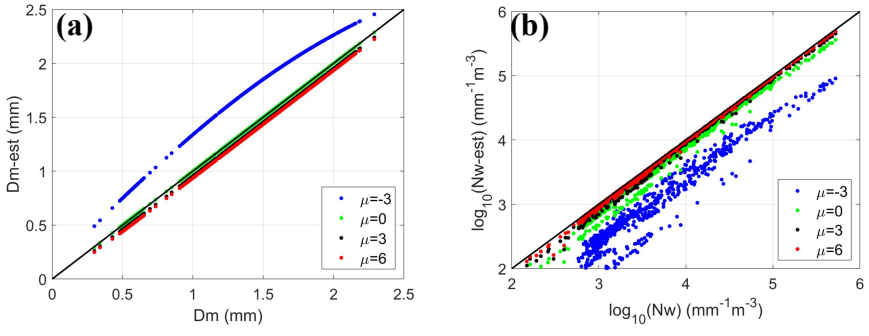

Figure 10. Sensitivity test of μ (a: retrieval of Dm; b: retrieval of Nw).

Table 5. Retrieval errors of Dm and Nw for different values of μ.

Parameter	μ	MB	MAE	RMSE
Dm	-3	0.3211	0.3211	0.3234
	0	0.0002	0.0004	0.0006
	3	-0.0466	0.0466	0.0466
	6	-0.0639	0.0639	0.0639
Nw	-3	-0.7067	0.7067	0.7414
	0	-0.1609	0.1609	0.1809
	3	-0.0684	0.0684	0.0819
	6	-0.0316	0.0316	0.0412

3.6 Compression the Ambiguous zone of DFR-Dm

Based on scattering simulations using the measured DSDs, the true reflectivities at X-, Ka-, and W-bands (denoted as Z_X, Z_{Ka}, and Z_W) were derived. These values were then used to compute the corresponding dual-frequency ratios [DFR(X, Ka) and DFR(Ka, W)]. As noted earlier, the relationship between DFR and Dm exhibits ambiguity when DFR is less than 0. This

https://doi.org/10.5194/egusphere-2026-174
Preprint. Discussion started: 23 February 2026

issue is illustrated in Fig. 11a: while a unique Dm value corresponds to each positive DFR, an ambiguous zone emerges (marked by dashed lines in Fig. 11a) for negative DFR values, where a single DFR corresponds to two different Dm values. This region is referred to as the ambiguous zone in the study.

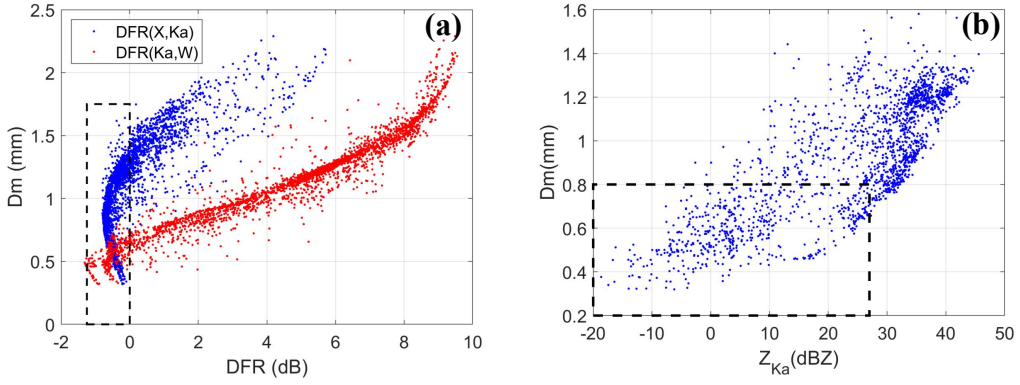

Figure 11. Scattering simulation scatterplots. (a) the DFR-Dm where blue dots represent DFR(X, Ka) and red dots represent DFR(Ka, W). The black dashed area indicates the ambiguous zone when DFR≤0. (b) the Z_{Ka}-Dm scatterplots when DFR(X, Ka)≤0, with the black dashed area representing the Z_{Ka}-Dm scatter plot when DFR(Ka, W)≤0.

Although the DFR(Ka, W)-Dm relationship also contains an ambiguous zone, its range is substantially narrower than that of DFR(X, Ka). As shown in Figure 11b, the ambiguous zone for DFR(Ka, W) is confined to a Z_{Ka} range of approximately −20 to 20 dBZ, corresponding to Dm values between 0.3 and 0.8 mm (dashed area). In comparison, the ambiguous zone for DFR(X, Ka) covers a much wider Z_{Ka} range of about −20 to 45 dBZ, corresponding to Dm values from 0.3 to 1.6 mm. Therefore, DFR(Ka, W) provides a more effective constraint on Dm retrievals, particularly where DFR(X, Ka)-Dm is ambiguous. This result validates the strategy adopted in this study: using DFR(Ka, W) to resolve ambiguities in the DFR(X, Ka)-Dm relationship.

Table 6 summarizes the statistics of the DFR data used in this study. The results show that 1,013 data points fall within the unambiguous zone of DFR(X, Ka) (>0), allowing unique retrieval of Dm. In comparison, the number increases significantly to 2,505 for DFR(Ka, W) (>0), demonstrating that DFR(Ka, W) effectively narrows the ambiguity zone associated with DFR(X, Ka). Relying solely on DFR(X, Ka), only 35.38% of the dataset yields a unique Dm solution. This proportion rises markedly to 87.5% when the constraint from DFR(Ka, W) is incorporated. These results confirm that DFR(Ka, W) substantially reduces retrieval ambiguity and improves the robustness of Dm retrieval.

Table 6. Dual-frequency ratio statistical results.

DFR	DFR＞0	DFR≤0	DFR	Proportion(DFR＞0)
DFR(X,Ka)	1013	1850	2863	35.38%
DFR(Ka,W)	2505	358	2863	87.50%

https://doi.org/10.5194/egusphere-2026-174
Preprint. Discussion started: 23 February 2026

4 Raindrop Size Distribution Retrieval and Evaluation

4.1 Retrieval of Dm

Given that DFR(Ka, W) exhibits a significantly narrower ambiguity zone than DFR(X, Ka), we leverage this characteristic to constrain and improve Dm retrieval. A combined approach has been formulated to resolve the ambiguity in the DFR(X, Ka)–Dm relationship. The derived relationship is presented in Fig. 12 and Eq. (17).

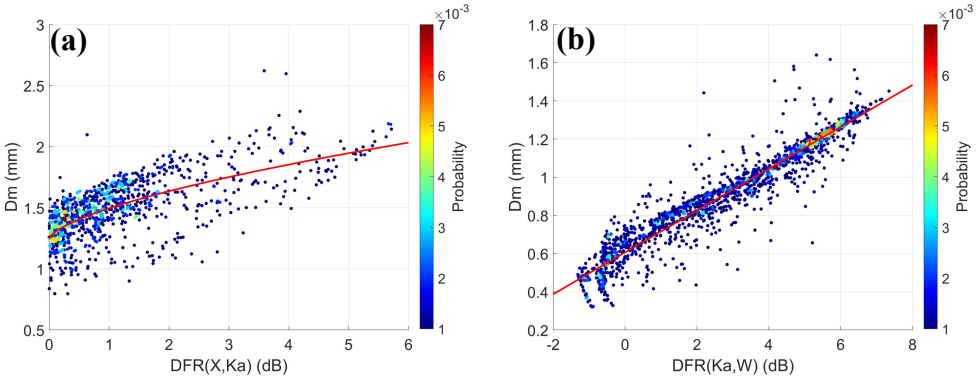

Figure 12. DFR-Dm fitting curve [a: DFR(X, Ka)>0, b: DFR(Ka, W) when DFR(X, Ka)≤0]

$$D_m = \begin{cases} 0.251DFR(X,Ka)^{0.6391} + 1.2445 & DFR(X,Ka) > 0 \\ 0.11DFR(Ka,W) + 0.6064 & DFR(X,Ka) \le 0 \end{cases} \quad (17)$$

As shown in Figure 12, the combination of DFR(X, Ka) and DFR(Ka, W) can accurately retrieve raindrops with Dm greater than 0.5 mm. Specifically, the DFR(Ka, W)–Dm accurately retrieves larger Dm values when DFR(Ka, W) is less than 0, with retrieval errors remaining only for raindrops smaller than 0.5 mm (Fig. 12b). Furthermore, as indicated in Fig. 13, rain rates do not exceed 0.6 mm h^{-1} when Dm is below 0.5 mm. Therefore, the retrieval error associated with DFR(Ka, W) in this range is almost negligible.

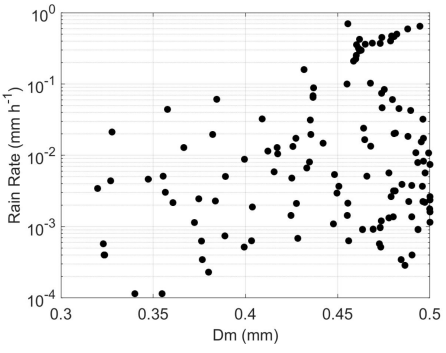

Figure 13. Scatterplots of rain rate versus Dm for cases where Dm ≤ 0.5 mm

https://doi.org/10.5194/egusphere-2026-174
Preprint. Discussion started: 23 February 2026

4.2 Retrieval of Nw and LWC

The normalized intercept parameter (Nw) is retrieved by Eq. (6), which depends on both LWC and Dm. While Dm is retrieved through the combination of DFR(X, Ka) and DFR(Ka, W), the retrieval of LWC is still required. In this study, the method proposed by Oh et al. (2018) is adopted to estimate LWC from Ka-band reflectivity.

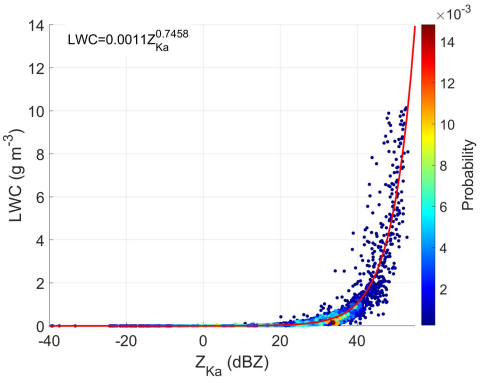

Figure 14. Scatterplots of the Ka-band reflectivity (Z_{Ka}) and liquid water content (LWC).

The fitted retrieval relationship between Z_{Ka} and LWC is presented in Fig. 14. This curve is derived from T-matrix scattering simulations based on measured raindrop size distributions. The monotonic and nonlinear nature of the Z_{Ka}-LWC relationship enables reliable LWC estimation over a broad dynamic range of the reflectivity.

4.3 Retrieval Results and Validation

To investigate the vertical structure of precipitation microphysics, Figure 15 shows retrieved profiles of Dm and Nw from X/Ka-band dual-frequency radar data. The results reveal distinct microphysical characteristics between convective and stratiform precipitation. Convective clouds generally exhibit larger Dm and Nw with significant vertical inhomogeneity, whereas stratiform clouds are more uniform. Notably, Dm increases at lower altitudes accompanied by a substantial enhancement in Nw in the convective regions. This indicates the occurrence of intense microphysical processes, such as raindrop coalescence and breakup, within convective updrafts and downdrafts.

In contrast, stratiform precipitation displays vertically uniform distributions of Dm and Nw, consistent with its stable, layered structure. However, the melting layer (bright band) causes a local enhancement in these parameters, leading to peaks in Dm and Nw near the 0 °C isotherm. This characteristic is attributed to the increased radar reflectivity of melting hydrometeors.

These findings demonstrate the effectiveness of the proposed retrieval method in capturing microphysical differences across precipitation types and vertical levels, offering valuable insights into cloud structure and precipitation formation mechanisms.

https://doi.org/10.5194/egusphere-2026-174
Preprint. Discussion started: 23 February 2026

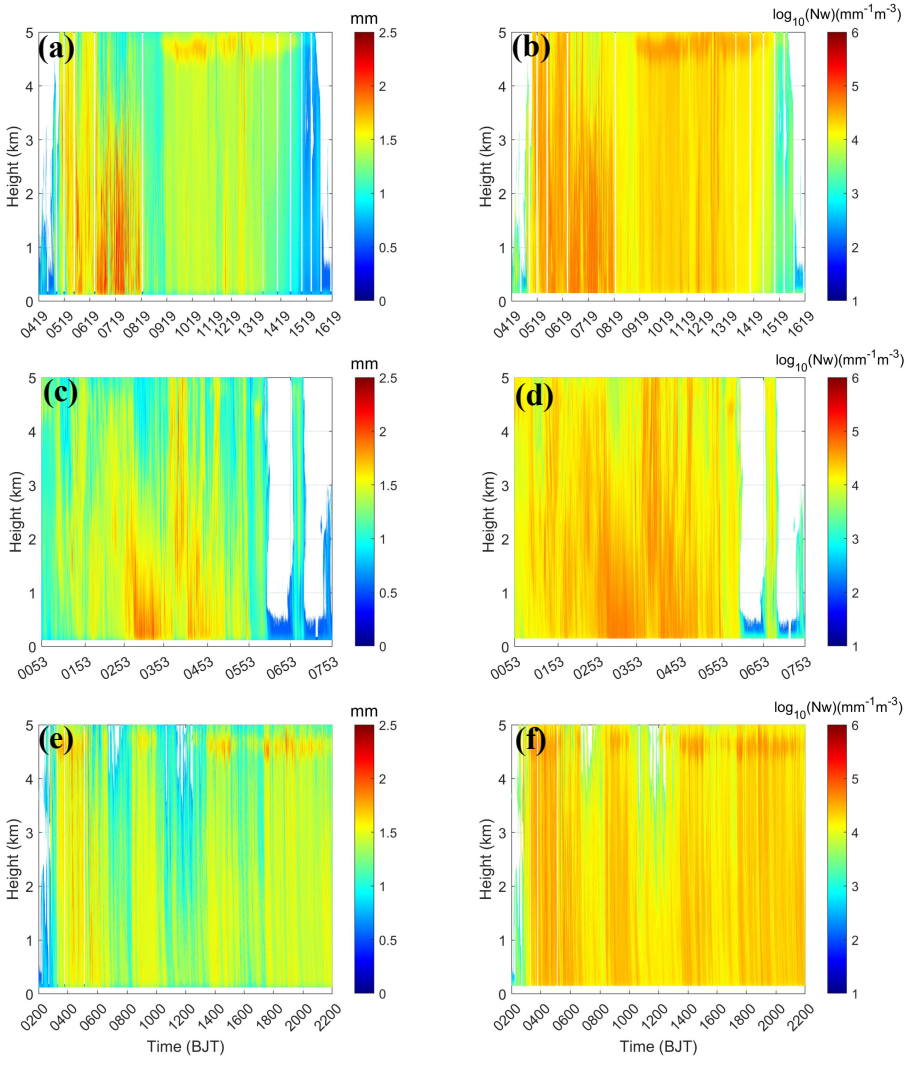

Figure 15. Time-height profiles of the mass-weighted mean diameter (Dm) and normalized intercept parameter (Nw). (Dm: a, c, e; Nw: b, d, f; top row: June 11, 2022; middle row: May 11, 2022; bottom row: May 1, 2022)

The performance of the proposed retrieval method was evaluated by comparing near-surface X/Ka-band radar retrievals with ground-based 2DVD observations. Its superiority was further demonstrated through a comparison with two conventional methods (Fig. 16) and the retrieval formula is shown in Eq. (18). The first estimates Dm only when DFR(X, Ka) > 0, ignoring the dual-solution problem (Wang et al., 2020; Liu et al., 2020). The second follows the same procedure as the first when DFR > 0, but it selects the large Dm when DFR ≤ 0 (Mardiana et al., 2004).

https://doi.org/10.5194/egusphere-2026-174
Preprint. Discussion started: 23 February 2026

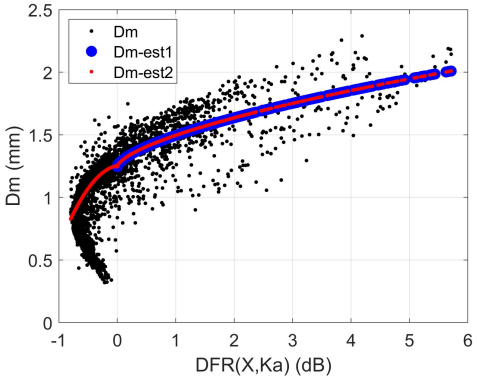

Figure 16. The mass-weighted mean diameter retrieved by conventional methods versus the true value. [Dm (black): true value; Dm-est1 (blue): the first conventional method; Dm-est2 (red): the second conventional method].

$$D_{m-est} = \begin{cases} 0.251DFR(X,Ka)^{0.6391} + 1.2445 & DFR(X,Ka) > 0 \\ -0.563DFR(X,Ka)^2 + 0.088DFR(X,Ka) + 1.254 & DFR(X,Ka) \le 0 \end{cases} \quad (18)$$

As shown in Figure 17, the first conventional method performs well only for large raindrops, but fails to capture Dm smaller than 1.3 mm (Fig. 17b). The second conventional method tends to overestimate the small Dm (Fig. 17c). In contrast, the proposed method demonstrates a substantial improvement by accurately retrieving Dm across the entire size spectrum (Fig. 17a), including smaller raindrops that are commonly found in stratiform and light precipitation.

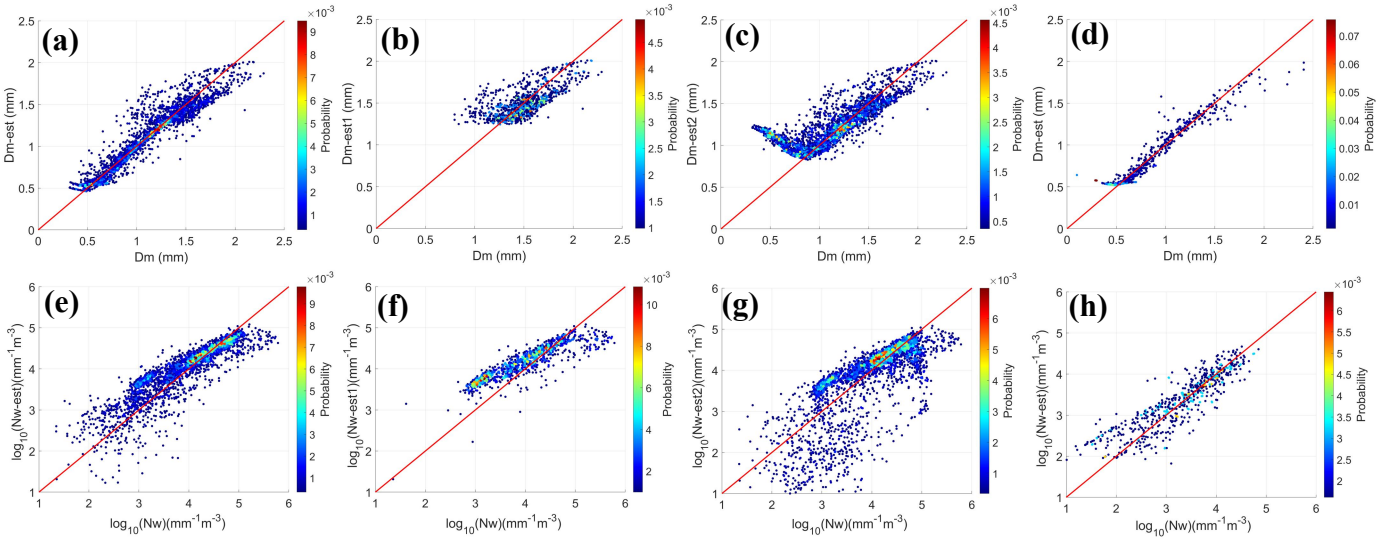

Figure17. Retrieved mass-weighted mean diameter (Dm) and normalized intercept parameter [log10(Nw)]. (a, e: the proposed method; b, f: the first conventional method; c, g: the second conventional method; d, h: the retrieved Dm and Nw of June 14, 2025 by the proposed method).

https://doi.org/10.5194/egusphere-2026-174
Preprint. Discussion started: 23 February 2026

In terms of Nw retrieval, the first conventional method can only accurately retrieve Nw for large raindrops (Fig. 17f). Due to the inverse relationship between Dm and Nw, the overestimation of Dm by the second conventional method leads to underestimated Nw retrievals for small raindrops (Fig. 17g). In contrast, the proposed method overcomes these limitations of conventional methods, demonstrating good consistency between the retrieved Nw and ground truth (Fig. 17e). Furthermore, the proposed method was applied to a precipitation case on June 14, 2025 to evaluate its applicability. As shown in Figures 17d and 17h, the retrieval results agree well with ground-based measurements, confirming the applicability of the proposed method. As quantitatively assessed in Table 7, the proposed method demonstrates good universality and superior accuracy in retrieving both Dm and Nw compared to the two conventional methods. Notably, despite the second conventional method performing better than the first for Dm retrieval, it shows weaker capability in retrieving Nw.

Table 7. Retrieval error statistics for the mass-weighted mean diameter (Dm) and the normalized intercept parameter (Nw). *Note: "-est" denotes results from the proposed method; "-est1" and "-est2" denote results from the first and second conventional methods, respectively; "-validation" denotes the retrieval results from the proposed method for June 14, 2025.*

Parameter	MB	MAE	RMSE	CC
Dm-est	-0.0016	0.0804	0.1242	0.9441
Dm-est1	-0.0004	0.1349	0.1491	0.6831
Dm-est2	0.0943	0.1762	0.2578	0.7829
Dm-validation	0.0321	0.0934	0.1490	0.9419
Nw-est	0.0671	0.2658	0.3662	0.8924
Nw-est1	0.1881	0.3529	0.4332	0.8761
Nw-est2	-0.1446	0.4530	0.6507	0.7504
Nw-validation	0.0676	0.2718	0.3673	0.8900

A comparison of retrieved raindrop size distributions with ground truth across reflectivity intervals is shown in Fig. 18. The proposed method outperforms the conventional ones, accurately retrieving DSDs across all intervals with particular improvement for weak echoes (Fig. 18a). While conventional methods improve with higher reflectivity (Figs. 18b-d), the proposed method consistently achieves the best accuracy, followed by the second and then the first conventional method. This conclusion is validated by the Dm and Nw error statistics (MB, MAE) in Fig. 19.

https://doi.org/10.5194/egusphere-2026-174
Preprint. Discussion started: 23 February 2026

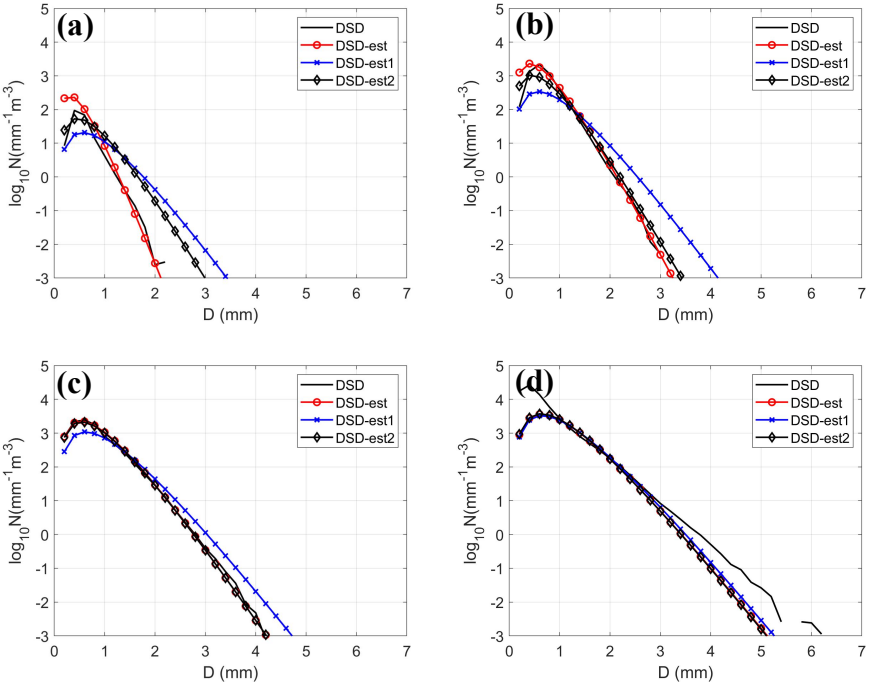

Figure 18. The mean raindrop size distributions retrieved by conventional methods (DSD-est1, DSD-est2) and the proposed method (DSD-est) against the true values (DSD). a: Z < 20 dBZ; b: 20 dBZ ≤ Z < 30 dBZ; c: 30 dBZ≤ Z < 40 dBZ; d: 40 dBZ ≤ Z < 50 dBZ.

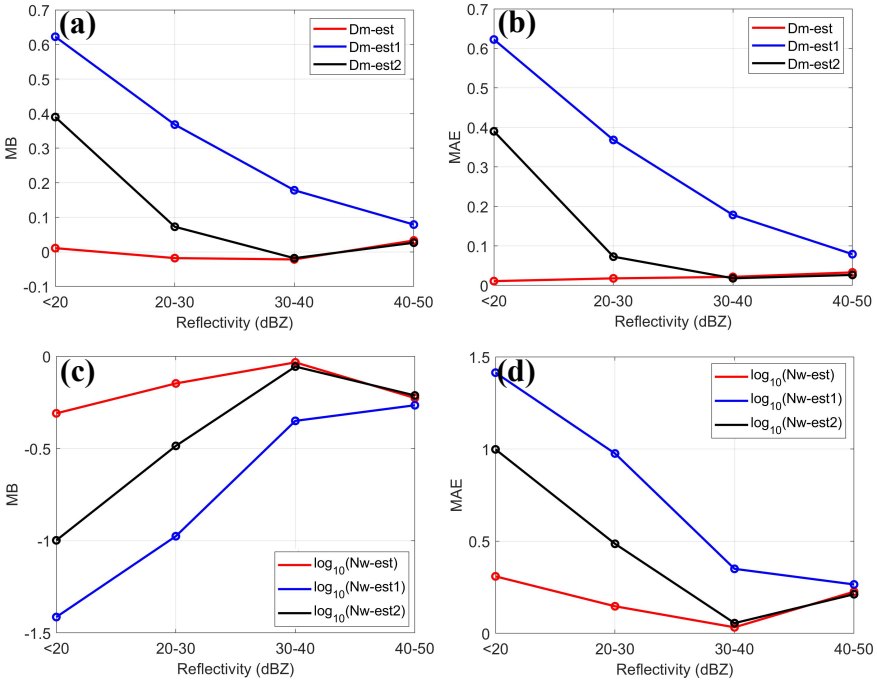

https://doi.org/10.5194/egusphere-2026-174
Preprint. Discussion started: 23 February 2026

Figure 19. Retrieval performance of Dm (a, b) and log10(Nw) (c, d) across multiple reflectivity intervals (-est, proposed method; -est1, first conventional method; -est2, second conventional method).

5 Conclusion and discussion

A improved raindrop size distribution retrieval method was developed based on T-matrix scattering simulations and vertically pointing X/Ka dual-frequency radar observations. This method was developed using three distinct precipitation cases from 2022 (occurring on May 1, May 11, and June 11) and was independently evaluated with data from June 14, 2025. The main findings are summarized as follows:

The DFR(Ka, W)-Dm can significantly reduce the ambiguity of DFR(X, Ka)-Dm. Specifically, the proportion of DFR(X, Ka) data capable of yielding a unique Dm solution increased from 35.38% to 87.5% after incorporating DFR(Ka, W). This improvement enables more accurate retrievals of Dm where DFR(X, Ka)≤0, significantly enhancing the robustness of dual-frequency Dm retrievals.

The DFR(Ka, W)-Dm relationship effectively resolves the large Dm (>0.5 mm) values when DFR(Ka, W)≤0, while the residual errors associated with small Dm in this regime are almost negligible. The proposed method demonstrates a substantial improvement in retrieving DSDs under weak reflectivity (20 dBZ), where conventional methods exhibit large retrieval errors, and produces accurate DSD estimations across a wide range of reflectivity.

It is important to note that the development of this retrieval framework is based on ground-based DSD data. While effective for near-surface retrievals, this approach may introduce uncertainties when applied to upper-level radar observations, due to possible discrepancies in microphysical characteristics between surface and elevated hydrometeors. Future work should address these limitations by incorporating height-dependent DSD models.

Code, data, or code and data availability

The dual-frequency radar data, raindrop size distribution data, and retrieval codes will be provided upon request from the corresponding author.

Author contributions

LF had the idea for the retrieval and wrote the manuscript. JY proposed improvements to the retrieval method and guided the writing of the manuscript. ZG has provided the joint observation data from dual-frequency radar and raindrop size distribution measurements. JS, YS, and HY provided valuable feedback during the development of the retrieval method and verification of the retrieval results.

https://doi.org/10.5194/egusphere-2026-174
Preprint. Discussion started: 23 February 2026

Competing interests

The contact author has declared that none of the authors has any competing interests.

Disclaimer

Copernicus Publications remains neutral with regard to jurisdictional claims made in the text, published maps, institutional affiliations, or any other geographical representation in this paper. While Copernicus Publications makes every effort to include appropriate place names, the final responsibility lies with the authors. Views expressed in the text are those of the authors and do not necessarily reflect the views of the publisher.

Acknowledgements

We gratefully acknowledge the Yangjiang Meteorological Bureau of Guangdong Province for providing the essential observational data and their dedicated efforts. We also extend our sincere thanks to the developers of the T-matrix scattering code, whose work made the scattering simulations in this research possible.

Financial support

This research is supported by the Frontier Research Program of the Chinese Academy of Sciences (XDB0760402).

Review statement

The review statement will be added by Copernicus Publications listing the handling editor as well as all contributing referees according to their status anonymous or identified.

References

Chang, A. T. C. and Wilheit, T. T.: Remote sensing of atmospheric water vapor, liquid water, and wind speed at the ocean surface by passive microwave techniques from the Nimbus 5 satellite, Radio Sci., 14, 793-802, https://doi.org/10.1029/RS014i005p00793, 1979.

Chudler, K., Rutledge S. A., and Dolan, B.: Unique radar observations of large raindrops in tropical warm rain during PISTON, Mon.Wea. Rev., 150, 2719-2736, https://doi.org/10.1175/MWR-D-21-0298.1, 2022.

Ellis, S. M. and Vivekanandan, J.: Liquid water content estimates using simultaneous S and Ka band radar measurements, Radio Science., 46, 1-15, https://doi.org/10.1029/2010RS004361, 2011.

https://doi.org/10.5194/egusphere-2026-174
Preprint. Discussion started: 23 February 2026

Feng, L., Xiao, H., and Luo, L.: Simulation of polarization characteristics and attenuation of dual-polarization rain-measuring radar with T-matrix methods, Chinese Journal of Computational Physics., 36, 189-202 (in Chinese), https://doi.org/ 10.19596/j.cnki.1001-246x.7826, 2019.

Hou, A. Y., Kakar, R. K., Neeck, S., and Coauthors.: The Global Precipitation Measurement Mission, Bull. Amer. Meteor. Soc., 95, 701–722, https://doi.org/10.1175/BAMS-D-13-00164.1, 2014.

Iguchi, T. and Meneghini, R.: Stability of the dual-frequency radar equations and a new method applied to the GPM's Dual-Frequency Precipitation Radar (DPR) data, IEEE Trans. Geosci. Remote Sens., 60, 5111818, https://doi.org/ 10.1109/TGRS.2022.3159396, 2022.

Iguchi, T., Seto, S., Meneghini, R., Yoshida, N., Awaka, J., Le, M., Chandrasekar, V., Brodzik, S., Kubota, T., and Takahashi, N.: GPM/DPR level-2 algorithm theoretical basis document, NASA ATBD, 238 pp, 2021.

Junyent, F., Chandrasekar, V., and Kennedy, P.: Resonance Scattering Detection Using the CSU–CHILL Dual-Wavelength, Dual-Polarization Radar, J. Atmos. Oceanic Technol., 36, 1177–1198, https://doi.org/10.1175/JTECH-D-18-0074.1, 2019.

Kubota, T., Seto, S., Satoh, M., Nasuno, T., Iguchi T., Masaki, T., Kwiatkowski, J. M., and Oki, R.: Cloud Assumption of Precipitation Retrieval Algorithms for the Dual-Frequency Precipitation Radar, J. Atmos. Oceanic Technol., 37, 2015–2031, https://doi.org/10.1175/JTECH-D-20-0041.1, 2020.

Ladino-Rincon, A., Nesbitt, S. W., Girolamo, L. D., Rauber, R. M., Mcfarquhar, G. M., and Lawson, R. P.: Droplet size distribution retrieval from dual-frequency precipitation radar measurement using a deep neural network, J. Atmos. Oceanic Technol., 42, 1549-1566, https://doi.org/10.1175/JTECH-D-25-0004.1, 2025.

Li, H., Ran, Z., Liu, L., Chen, Y., Bi, Y., Zhang, Y., Chen, H., and Mao J.: Research progress in profiling cloud and precipitation microphysics characteristic with ground-based multi-frequency radar, Torrential Rain and Disasters, 42, 361-371(in Chinese), https://doi.org/ 10.12406/byzh.2023-075, 2023.

Liao, L. and Meneghini, R.: Physical evaluation of GPM DPR single- and dual-wavelength algorithms, J. Atmos. Oceanic Technol., 36, 883–902, https://doi.org/10.1175/JTECH-D-18-0210.1, 2019a.

Liao, L. and Meneghini, R.: A modified dual-wavelength technique for Ku- and Ka-band radar rain retrieval, J. Appl. Meteor. Climatol. , 58, 3–18, https://doi.org/10.1109/IGARSS.2018.8517440, 2019b.

Liao, L., Meneghini, R., and Tokay, A.: Uncertainties of GPM DPR rain estimates caused by DSD parameterizations, J. Appl. Meteor. Climatol., 53, 2524–2537, https://doi.org/10.1175/JAMC-D-14-0003.1, 2014.

Liao, L. and Meneghini, R.: A study of air/space-borne dual-wavelength radar for estimates of rain profiles, Adv. Atmos. Sci., 22, 841–851, https://doi.org/10.1007/BF02918684, 2005.

Liebe, H. J.: An updated model for millimeter wave propagation in moist air, Radio Sci., 20, 1069-1089, https://doi.org/ 10.1029/RS020i005p01069, 1985.

Liu, L., Zhang,Y., and Ding, H.: Vertical air motion and raindrop size distribution size distribution retrieval using a Ka/Ku dual-wavelength cloud radar and its preliminary application, Chinese Journal of Atmospheric Sciences, 45, 1099−1113(in Chinese), doi:10.3878/j.issn.1006-9895.2104.20200, 2021.

https://doi.org/10.5194/egusphere-2026-174
Preprint. Discussion started: 23 February 2026

Liu, S. and Wang G.: Study on the impacts of DSD parameters on precipitation estimation using dual-frequency radar, Plateau Meteorology, 39, 570-580(in Chinese), https://doi.org/10.7522/j.issn.1000-0534.2019.00092, 2020.

Mardiana, R., Iguchi, T., and Takahashi, N.: A dual-frequency rain profiling method without the use of a surface reference technique, IEEE Trans. Geosci. Remote Sens., 42, 2214–2225, https://doi.org/10.1109/TGRS.2004.834647, 2004.

Marshall, J. S. and Palmer, W. M.: The distribution of raindrops with size, J. Meteor., 5, 165-166, https://doi.org/10.1175/1520-0469(1948)005<0165:TDORWS>2.0.CO;2, 1948.

Meneghini, R., Liao, L., and Iguchi, T.: A Generalized Dual-Frequency Ratio (DFR) Approach for Rain Retrievals, J. Atmos. Oceanic Technol., 39, 1309–1329, https://doi.org/10.1175/JTECH-D-22-0002.1, 2022.

Meneghini, R., Kozu, T., Kumagai, H., and Boncyk, W. C.: A study of rain estimation methods from space using dual-wavelength radar measurements at near-nadir incidence over ocean, J. Atmos. Oceanic Technol., 9, 364–382, https://doi.org/ 10.1175/1520-0426(1992)009<0364:ASOREM>2.0.CO;2, 1992.

Meneghini, R., Kumagai, H., Wang, J. R., Iguchi, T., and Kozu, T.: Microphysical retrievals over stratiform rain using measurements from an airborne dual-wavelength radar-radiometer, IEEE Trans. Geosci. Remote Sens., 35, 487–506, https://doi.org/10.1109/36.581956, 1997.

Oh, S. B., Lee, Y. H., Jeong, J. H., Kim, Y. H., and Joo, S.: Estimation of the liquid water content and Z–LWC relation using Ka-band cloud radar and a microwave radiometer, Meteorol. Appl., 25, 423–434, https://doi.org/10.1002/met.1710, 2018.

Rose, C. R. and Chandrasekar, V.: A system approach to GPM dual-frequency retrieval. IEEE Trans. Geosci. Remote Sens., 43, 1816–1826, https://doi.org/10.1109/TGRS.2005.851165, 2005.

Seto, S., Iguchi, T., Meneghini, R., Awaka, J., Kubota, T., Masaki, T., and Takahashi, N.: The precipitation rate retrieval algorithms for the GPM Dual-Frequency Precipitation Radar, J. Meteor. Soc. Japan., 99, 205–237, https://doi.org/10.2151/jmsj.2021-011, 2021.

Seto, S., Iguchi, T., and Oki, T.: The basic performance of a precipitation retrieval algorithm for the Global Precipitation Measurement mission's single/dual-frequency radar measurements, IEEE Trans. Geosci. Remote Sens., 51, 5239–5251, https://doi.org/10.1109/TGRS.2012.2231686, 2013.

Skofronick-Jackson, G. and Coauthors.: The Global Precipitation Measurement (GPM) mission for science and society, Bull. Amer. Meteor. Soc., 98, 1679–1695, https://doi.org/10.1175/BAMS-D-15-00306.1, 2017.

Skofronick-Jackson, G., Kirschbaum, D., Petersen, W., Huffman, G., Kidd, C., Stocker, E. and Kakar, R.: The Global Precipitation Measurement (GPM) mission's scientific achievements and societal contributions: Reviewing four years of advanced rain and snow observations, Quart.J.Roy.Meteor.Soc., 144,27–48, https://doi.org/10.1002/qj.3313, 2018.

Tang, Q., Xiao, H., Guo, C., and Feng, L.: Characteristis of the raindrop size distributions and their retrieved polarimetric radar parameters in northern and southern China, Atmos. Res., 135-136, 59-75, https://doi.org/10.1016/j.atmosres.2013.08.003, 2014.

https://doi.org/10.5194/egusphere-2026-174
Preprint. Discussion started: 23 February 2026

Testud, J., Oury, S., Amayenc, P., and Black, R. A.: The concept of "normalized" distributions to describe raindrop spectra: A tool for cloud physics and cloud remote sensing, J. Appl. Meteor., 40, 1118–1140, https://doi.org/10.1016/S 1464-1909(00)00122-2, 2001.

Tokay, A. and Beard, K. V.: A Field Study of Raindrop oscillations. Part I: Observation of Size Spectra and Evaluation of Oscillation Causes, J. Appl. Meteor., 35, 1671-1687, https://doi.org/10.1175/1520-0450(1996)035<1671:AFSORO>2.0.CO;2, 1996.

Ulbrich, C. W.: Natural variations in the analytical form of the raindrop size distribution, J. Climate Appl. Meteor., 22, 1764–1775, https://doi.org/10.1175/1520-0450(1983)022<1764:NVITAF>2.0.CO;2, 1983.

Wang, G., Liu, S., and Liu, L.: Uncertainties in retrieving microphysical properties of rain profiles using ground-based dual-frequency radar, Meteorol. Appl., 27, e1876, https://doi.org/10.1002/met.1876, 2020.

Waterman, P. C.: Matrix formulation of electromagnetic scattering, Proc. IEEE., 53, 805-812, https://doi.org/ 10.1109/ PROC.1965.4058, 1965.

Waterman, P. C.: Symmetry, unitarity and geometry in electromagnetic scattering, Phys. Rev., 3, 825-839, https://doi.org/10.1103/PhysRevD.3.825, 1971.